Experimental study of resonance states in ^{7}H and ^{6}H

M. Caamaño,[1,2,*] D. Cortina-Gil,[1] W. Mittig,[2] H. Savajols,[2] M. Chartier,[3] C. E. Demonchy,[2] B. Fernández,[3] M. B. Gómez Hornillos,[3] A. Gillibert,[4] B. Jurado,[2] O. Kiselev,[5,6] R. Lemmon,[7] A. Obertelli,[4] F. Rejmund,[2] M. Rejmund,[2] P. Roussel-Chomaz,[2] and R. Wolski[8]

[1]*Department of Particle Physics, Universidade de Santiago de Compostela, E-15782, Santiago de Compostela, Spain*

[2]*GANIL CEA/DSM-CNRS/IN2P3, BP 55027, F-14076 Caen Cedex 05, France*

[3]*Department of Physics, University of Liverpool, Oliver Loge Laboratory, L69 7ZE Liverpool, United Kingdom*

[4]*CEA/DSM/IRFU, CEA Saclay, F-91191 Gif sur Yvette Cedex, France*

[5]*Paul Scherrer Institut, CH-5232 Villigen, Switzerland*

[6]*PNPI, Gatchina RU-188300, Russia*

[7]*CCLRC Daresbury Laboratory, Warrington, Cheshire, WA4 4AD, United Kingdom*

[8]*Henryk Niewodniczański Institute of Nuclear Physics, ul. Radzikowskiego 152 PL-31-342 Krakow, Poland*

(Received 3 July 2008; published 10 October 2008)

The ^{7}H and ^{6}H nuclear systems were investigated via transfer reactions with a ^{8}He beam at 15.4A MeV impinging in a ^{12}C target. The experimental setup allowed a complete reconstruction of the reaction kinematics with the MAYA gas detector, based on the active-target concept, where the carbon atoms of the filling isobutane played also the role of reaction target. The ^{7}H resonance was observed at $0.57^{+0.42}_{-0.21}$ MeV above the $^{3}\mathrm{H} + 4n$ threshold with a width of $0.09^{+0.94}_{-0.06}$ MeV. The ^{6}H system was formed at $2.91^{+0.85}_{-0.95}$ MeV with a resonance width of $1.52^{+1.77}_{-0.35}$ MeV. These results show the availability of nuclear structure information well outside the bounding limits, resulting in an extraordinary input to improve the present models and understanding of nuclear matter.

DOI: 10.1103/PhysRevC.78.044001 PACS number(s): 27.20.+n, 25.60.Je, 25.70.Ef

I. INTRODUCTION

Nearly all our present knowledge about nuclear matter is based on properties extracted from spectroscopy and reactions with stable nuclei. Recent improvements in the production of radioactive beams allow to test the current nuclear models in regions far from stability never explored. As a result, many new phenomena are being found, improving and modifying the understanding of nuclear matter behavior in order to include the new observations. Studies far from stability are relatively accessible for light nuclei, where the drip lines are reached with the addition or removal of only a few neutrons in the stable isotopes. In case of hydrogen and helium the exploration can be extended out of the drip line limits, where nuclear systems are found in the form of resonances. The study of these resonances may show important features of the interaction between nucleons.

The case of light nuclei is interesting because the relatively low number of involved nucleons also pushes the development of pioneering theoretical descriptions that take into account the individual interactions between them, as well as the influence of the inner structure of the systems. For example, *ab initio* calculations [1,2] have shown the importance of taking into account multibody interactions when applying realistic nucleon-nucleon forces. In other approaches, the loosely bound character of the additional nucleons is the base for a core coupled to individual nucleons [3], or cluster structures [4,5]. The coupling of different channels, and particularly with the continuum, is also important [6], and models based on a shell model approach have proved to be successful in this region with relatively accurate predictions on the binding energy of these systems [7,8].

The experimental study of hydrogen isotopes heavier than tritium is a suitable probe for these theoretical approaches. Heavy hydrogen isotopes are accessible for more than 40 years [9]. However, the isotopic chain is far from being complete and understood. Whereas experiments have reported the existence of ^{4}H, ^{5}H, and ^{6}H as resonances [10–14], their fundamental properties are not unambiguously determined. In this situation, the search for new members of the isotopic chain aims to shed light on these problems, such as the evolution of the binding energy with the number of neutrons. In addition, these resonances represent the most exotic nuclear systems, with neutron to proton ratios $N/Z \geqslant 3$.

The existence of the ^{6}H resonance was reported in mid-1980s with the study of ^{7}Li(^{7}Li, ^{8}B)^{6}H at 82 MeV [14], and ^{9}Be(^{11}B, ^{14}O)^{6}H at 88 MeV [10]. A later attempt with π double charge exchange reaction ^{6}Li(π, π^{+})X [15] reported no evidence for the formation of the ^{6}H resonance, whereas a recent experiment showed a collection of ground and excited states in a higher energy domain from π^{-} absorption reactions [16]. In addition, different theoretical approaches range from the possibility of a bound ^{6}H system [17], a low-lying state [1] to the absence of any resonance [18], leaving an open question about its existence. The same approximations were also applied to the ^{7}H system with similar contradictory results. However, more recent theoretical calculations agreed in predicting the ^{7}H system as a resonance with an energy above the $^{3}\mathrm{H} + 4n$ mass varying from around 1 MeV [7] up to 7 MeV [1]. In parallel, experimental studies showed a sharp increase in the cross section of the $p(^{8}\mathrm{He}, pp)$ channel close to the $^{3}\mathrm{H} + 4n$ disintegration threshold [19], interpreted as a first tentative evidence of the existence of ^{7}H as a low

*caamano@ganil.fr

lying resonance. The present work confirms the properties of ^{6}H, while describing in more details the observation of the ^{7}H system, already reported in [20], along with its characterization.

II. EXPERIMENTAL SETUP

The experiment was performed at GANIL (France) using the SPIRAL facility based on the Isotope Separation On Line (ISOL) technique [21] of beam production. A secondary beam of ^{8}He at 15.4A MeV, with an intensity of $\sim 10^{4}$ pps, was produced from a primary ^{13}C beam on a thick ^{12}C target. The resulting beam of ^{8}He impinged on a isobutane (C_4H_{10}) gas target. From the collisions of the ^{8}He with the ^{12}C of the gas, the ^{7}H system was studied via ^{12}C(^{8}He, $^{7}\mathrm{H} \rightarrow {}^{3}\mathrm{H} + 4n$)^{13}N, whereas the ^{6}H resonance was produced in the ^{12}C(^{8}He, $^{6}\mathrm{H} \rightarrow {}^{3}\mathrm{H} + 3n$)^{14}N transfer reaction.

The experimental setup allowed to detect the charged particles involved in the reaction using the active-target MAYA [22–24]. This device is specially well-suited for detecting reaction products in a very low energy domain. The detector works as a time-charge projection chamber where the detection gas plays also the role of reaction target, and the trajectory and energy loss of the particles are determined.

Figure 1 shows the detection setup. Two main zones can be identified within the MAYA detector: an active volume of $28 \times 26 \times 20$ cm^3 where the reaction takes place, and the amplification area where detection and readout occur. The amplification zone consists of a Frisch grid, an anode wire plane below, and a segmented cathode in the lower part. The cathode is segmented into 35×35 hexagonal pads, each of which measures 5 mm per side. The pads are arranged in rows parallel to the anode wires; the signals are individually read and coded.

In general, the detection occurs when the beam particles and the reaction products ionize the filling gas along their paths. The electrons released in the ionization process drift toward the amplification area, where they are accelerated around the wires. A mirror charge is induced on the corresponding pads of the segmented cathode.

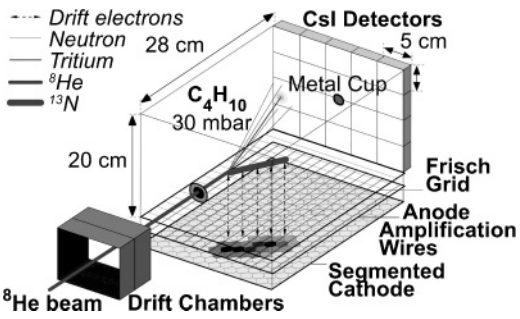

FIG. 1. Experimental setup. Two drift chambers, in front of the MAYA detector, monitor the beam particles. The reactions occur in the volume filled with C_4H_{10} gas. A 5×5 matrix of CsI detectors is placed at the back side for detecting light particles. A small metal cup is used to stop the beam.

Measurements of the drift time of the ionizing electrons up to the amplification wires allow to calculate the vertical position. This information is combined with the reconstruction of trajectories projected on the cathode plane to perform a complete three-dimensional tracking of those reaction products that lose enough energy to be detected. A segmented wall of twenty cesium-iodide (CsI) crystals placed at forward angles detects those particles that do not stop inside the gas volume. The detection of a charged particle in any CsI detector is used for triggering the data acquisition system during the experiment. Two drift chambers located before MAYA are used as beam monitors. The nonreacting beam projectiles are stopped in a small metal cup at the end of MAYA.

III. DATA ANALYSIS

In a typical event a ^{8}He projectile enters the detector and reacts with a ^{12}C of the isobutane used as filling gas. In the present experiment, the isobutane was at a pressure of 30 mbar, which corresponds to a target thickness of 3.2×10^{19} ^{12}C/cm^2. The transfer of a proton between the ^{8}He and ^{12}C may produce the ^{7}H system, whereas the transfer of one proton and one neutron may form the ^{6}H system. The scattering ^{6}H or ^{7}H decays immediately into a ^{3}H with relatively high kinetic energy (around 10 MeV/nucleon) and three or four neutrons. The difference between triton and nitrogen recoil kinematics results in very different energy loss and does not allow to stop both reaction residues in the gas with measurable ranges within the same pressure. The pressure of the filling gas was chosen to stop the heavy recoils inside the active volume, where their range and angle were measured using the charge image projected on the segmented cathode. In the case of recoil nitrogen from $1p$ and $1p1n$ transfers, typical ranges are of the order of 8 cm, corresponding to $\sim$10 MeV, with angles between 30 and 50 deg. On the other hand, the light scattering particles do not leave enough energy in the gas for being detected in the segmented cathode. They traverse the active volume toward the CsI wall, where they are stopped and identified.

The charges collected in the pads form an image of the energy loss of the recoil along its path inside the gas. From these charges the angle and range of the recoil can be recovered. The recoil angle projected in the cathode plane is calculated with a fit of the points where maxima of charge deposition are found. The pads with maximum charge are searched along the three axes of symmetry of the hexagonal pads. Figure 2 shows the localization of these maxima in a real event. The positions of these points are corrected with a center of gravity procedure based on the secant hyperbolic function [25]. The trajectory is fitted from the resulting positions in order to obtain its angle projected on the cathode plane. The process is repeated for each symmetry axis in order to chose the most accurate trajectory according to the fit quality. The accuracy in the final positions is around 1 mm, which results in an uncertainty for the projected angle lower than 1°.

The charges collected in the pads are also used to build the energy loss profile of the particle. The profile is the projection in the preferred axis of symmetry of the deposited charge. It shows the evolution of the energy loss along the trajectory in

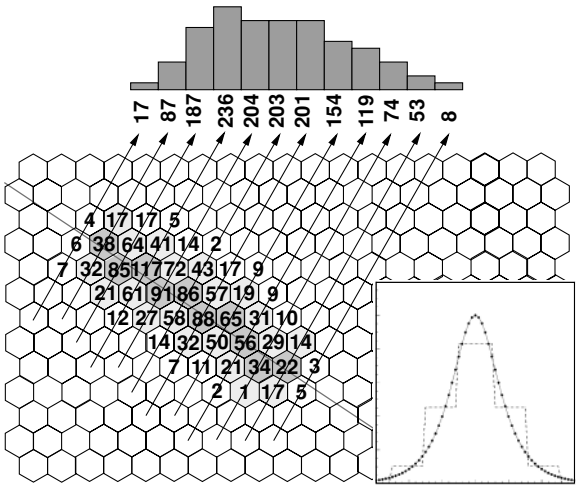

FIG. 2. Construction of charge profile. The figure shows an area of the segmented cathode with a particle trace, represented by the grey crossing line. The numbers in the pads correspond to the charge collected. Those pads with the maxima of charge collected along the selected axis of symmetry are signalled in dark grey. The total charge collected in each row along this axis is used to build the charge profile depicted in the upper part of the figure. The inset shows the punctual charge induction with the connected points, and its projection in a row of pads with a dashed line.

fixed steps. The process is reviewed in Fig. 2 with the charge pattern collected in a real event. The projected range is obtained from the energy loss profile as the distance between the vertex of reaction and the ending point of the trajectory.

A particular characteristic of the calculated energy profiles is the absence of the Bragg peak at the ending point, due to the low energy of the recoil products. This situation forces a specific treatment based on simulations performed under realistic conditions of energy loss and charge induction (see Fig. 3): an energy loss profile along the trajectory, calculated with the code TRIM [26], is convoluted with the induction from a punctual charge [27]. The resulting charge distribution is projected onto the pads for different positions of the trajectory (with the trajectory starting between two pads, starting in the middle of one pad, etc.). From these simulations, a mathematical formula is deduced to calculate the starting and ending point of the trajectory with the charge collected in the pads. The starting point is determined using the first three steps of the charge profile:

$$Pos_{\text{vertex}} = \frac{pos_1 + pos_2}{2} + CoG_{\text{vertex}} \tag{1}$$

with pos_i as the position of the ith step of the charge profile, and

$$CoG_{\text{vertex}} = \frac{\delta q_0 - \delta q_2}{\delta q_0 + \delta q_1 + \delta q_2}\,\delta q_i = q_{i+1} - q_i, \tag{2}$$

where q_i is the charge in the ith step of the charge profile, and $q_0 = 0$. The ending point is calculated with the last two steps of the charge profile $q_{\text{second-last}}$ and q_{last}:

$$Pos_{\text{range}} = Pos_{\text{last}} + \frac{\Delta x_{\text{axis}}}{2} CoG_{\text{range}} \tag{3}$$

with Δx_{axis} being the distance between two consecutive steps, or, equivalent, the distance between two rows of pads. The CoG_{range} is

$$CoG_{\text{range}} = \frac{\delta q_{\text{last}} - \delta q_{\text{second-last}}}{\delta q_{\text{second-last}} + \delta q_{\text{last}}}. \tag{4}$$

The estimated uncertainty for this method is 1.4 mm in the range calculation. Finally, the projected ranges and angles are corrected with the reaction plane angle, measured with the drift time up to each anode wire. The drift times are translated to distances, through the drift velocity of the electrons in the gas, and fitted to obtain the reaction plane angle with a resolution around 7°. It is important to note that the final uncertainties for recoil ranges and angles depend on the characteristics of each event, with typical values around 5 mm and 1°, respectively. The energy of the recoil, once identified, is given by its range and calculated with codes as SRIM [26] with a resolution better than 5%.

The first step in the selection of the ^{12}C(^{8}He, ^{6,7}H $\rightarrow$ ^{3}H + $(3,4)n$)^{14,13}N channels consists in the coincident identification of the charged reaction products, tritium and nitrogen. Figure 4 shows an approximation of the kinematical region covered by the geometry of the detector. The angular range of detection for the nitrogen recoil is within ~30–50° with an energy approximately between 3 and 20 MeV in laboratory frame.

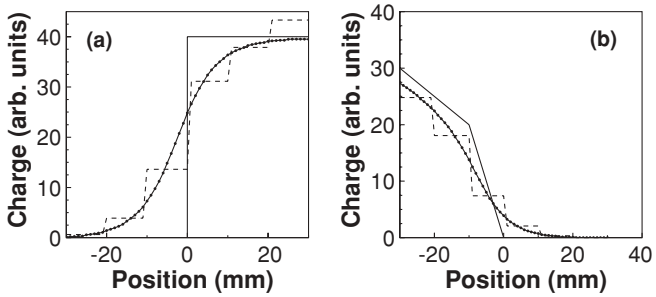

FIG. 3. Simulation of (a) starting and (b) ending points of energy loss profile. The energy loss along the trajectory is schematically described by the solid line. The connected points correspond to the convolution of the energy loss with the distribution of induction from a punctual charge. The dashed line builds the charge profile with the projection of the charge distribution in a row of pads.

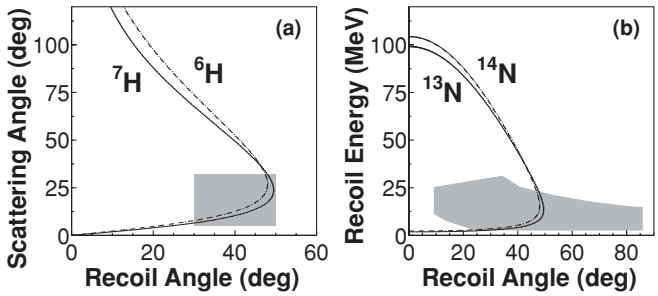

FIG. 4. Kinematics of ^{7}H and ^{6}H production. (a) Scattering angle of ^{7}H (solid line) and ^{6}H (dashed line) respect to recoils ^{13}N and ^{14}N in laboratory. (b) Kinematics of recoils ^{13}N (solid line) and ^{14}N (dashed line). The grey area corresponds to the geometrical coverage of MAYA in both panels.

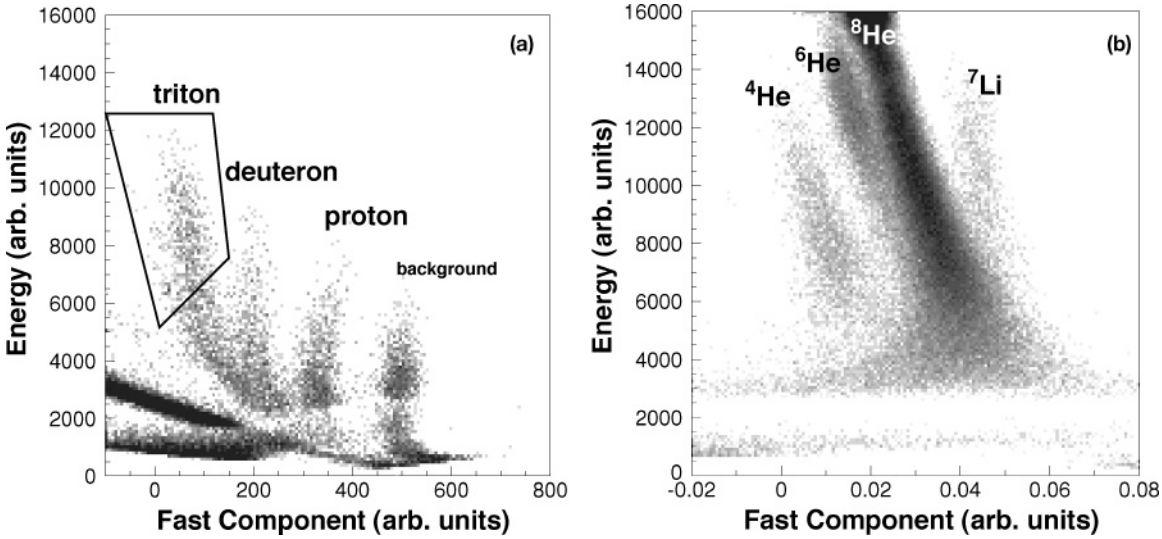

FIG. 5. Identification of light scattering particles in CsI. The total energy in the CsI detectors is plotted versus the fast component of the signals. (a) shows the identification of $Z = 1$ isotopes. The solid line shows a selection where high energy tritons involved in $1p$-xn transfer reactions are expected. (b) Identification of $Z \geqslant 2$ isotopes.

The detection of the light scattering partner is done in the segmented CsI wall, with an angular coverage between ∼5 and 35°. In the case of ^{6,7}H, the scattering partner decays into $^{3}\mathrm{H} + (3, 4)n$, being the triton detected in the CsI wall. The decay of ^{6,7}H, either sequential or in one step, contributes in less than 0.05° in deviating the ^{3}H from the original ^{6,7}H trajectory. The angular window resulting from the CsI detection contributes to a slight reduction of the observed kinematical region of the nitrogen to around 5–15 MeV when detected in coincidence with the scattering triton. In Sec. III B the kinematical limits for the detection of the ^{7}H and ^{6}H production are given in more detail.

The stopped triton in the segmented CsI wall is identified via the relation between the total energy and the fast component of the CsI signal output, which is sensitive to the mass and charge of the particle [28]. Figure 5 shows this relation to identify hydrogen, helium and lithium isotopes produced in different reactions inside MAYA for a specific set of experimental data.

The nitrogen recoil, with a total energy between 3 and 15 MeV, corresponding to ranges between 40 and 160 mm, is stopped inside the detector, where the identification is done by means of the relation between the measured range and the deposited charge. This relation is a particular function of the total energy for each ionizing particle when it is completely stopped inside the gas. Figure 6 shows the identification of nitrogen among other recoil species by means of their different range over charge ratios. The largest contribution corresponds to carbon isotopes coming from elastic reactions. Higher range over charge ratios are populated with isotopes with lower charges, such as boron isotopes produced in $^{12}\mathrm{C}(^{8}\mathrm{He}, {}^{x}\mathrm{Li})^{20-x}\mathrm{B}$ reactions. The left peak corresponds to charges greater than carbon, which, in the present case, can only be populated with nitrogen isotopes. The grey histogram in Fig. 6 shows the distribution conditioned by the detection in one of the CsI detectors of a triton in the selection shown in Fig. 5. Events corresponding to carbon isotopes are still present after the condition, mainly due three-body reaction channels. Nevertheless, the good separation between carbon and nitrogen when the tritium coincidence is applied allows to remove any contamination from these channels.

A. Identification of ^{6}H and ^{7}H events

The different $1p$-xn transfer reactions producing ^{3}H and a nitrogen recoil are separated by their different kinematics. Contributions from other reaction channels, such as fusion-evaporation, are eliminated with the coincident detection of a single recoil, identified as nitrogen, and a single scattering particle in the CsI wall, identified as a triton with relatively high energy.

The $^{12}\mathrm{C}(^{8}\mathrm{He}, {}^{6,7}\mathrm{H})^{14,13}\mathrm{N}$ transfer are binary reactions with two particles in the final state. Conservation of energy and momentum allows to reconstruct the reaction with kinematic

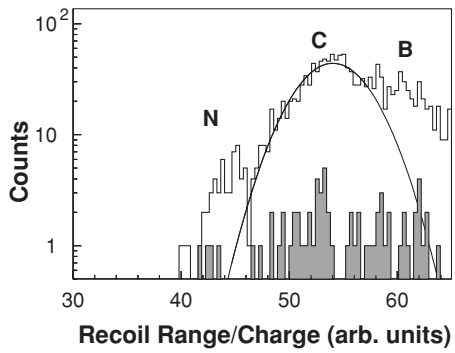

FIG. 6. Recoil nitrogen identification. The selection of nitrogen among other recoil species is shown in a spectrum of range/charge ratio. The carbon isotopes region is fitted to a Gaussian shape for reference. The grey histogram shows the distribution when conditioned by tritium identification in one of the CsI detectors.

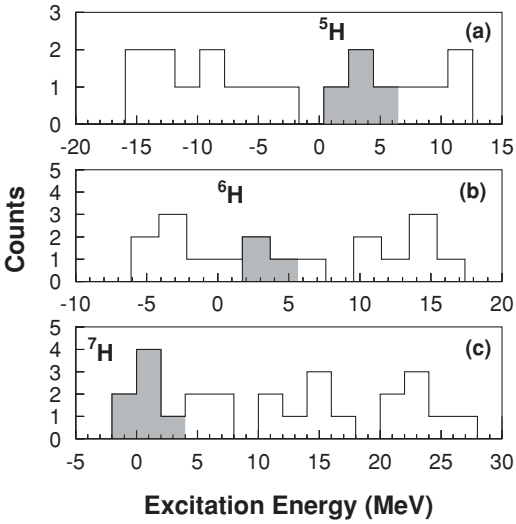

FIG. 7. Excitation energy distributions calculated under the assumptions of (a) ^{5}H, (b) ^{6}H, and (c) ^{7}H production channels. The grey histograms in the ^{5}H and ^{6}H channels correspond to those events lying in the regions where the resonances were already observed in previous experiments. The grey histogram in the ^{7}H corresponds to those events identified as ^{7}H production. See text for details.

information from only one of the reaction products. In the present work, the reconstruction is done with the nitrogen recoil angles and energies measured with the three-dimensional tracking of MAYA. The excitation energy distribution of the ^{6}H and ^{7}H systems can be obtained from the kinematical information applying a missing mass calculation. The excitation energy is then defined as the difference between the calculated mass of the ^{6}H and ^{7}H systems with respect to each $^{3}\mathrm{H} + 3n$ and $^{3}\mathrm{H} + 4n$ subsystem masses, respectively.

The identification of the ^{7}H and ^{6}H events is done after the identification of the events corresponding to the different reaction channels with ^{3}H and nitrogen as products. For completeness, the production of ^{5}H through a $1p$-$2n$ is also investigated. Panel (a) in Fig. 7 shows the excitation energy distribution corresponding to ^{5}H production. This is calculated assuming that the detected nitrogen is ^{15}N and the subsystem mass corresponds to $^{3}\mathrm{H} + 2n$. The region in full grey is defined by the width of the ^{5}H resonance and centered in its energy, according to previous experiments [12,13]. Consequently, the events lying on this region are associated to the ^{5}H channel. Panel (b) shows the excitation energy distribution corresponding to ^{6}H production. The calculation was done assuming the detected nitrogen as ^{14}N and a $^{3}\mathrm{H} + 3n$ subsystem mass. Again, the full grey histogram corresponds to a region defined by the ^{6}H resonance width and energy observed in previous experiments [14]. The events in this region are different from those associated with ^{5}H and they are associated with the ^{6}H production. Finally, panel (c) shows the excitation energy distribution assuming the detected nitrogen as ^{13}N and the subsystem mass as $^{3}\mathrm{H} + 4n$. The events lying on the peak marked in grey around the $^{3}\mathrm{H} + 4n$ disintegration threshold are also different from those previously associated to ^{5}H and ^{6}H channels.

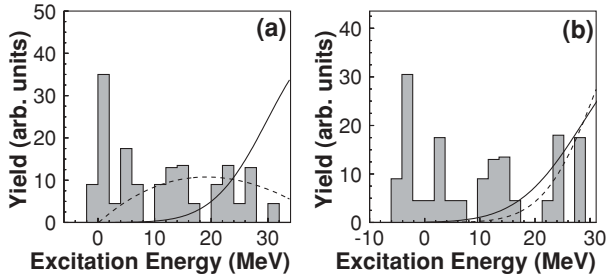

FIG. 8. Phase-space calculation. (a) The six-body (solid line) and three-body (dashed line) calculated phase-space are plotted over the excitation energy distribution associated with ^{7}H production. (b) The six-body phase-space from $1p$ transfer (solid) and five-body phase-space from $1p$-$1n$ transfer (dashed line) are plotted over the excitation energy distribution associated with ^{6}H production.

Contamination from other channels as fusion-evaporation is estimated in a population smaller than one count in the kinematic regions of ^{7}H and ^{6}H. Phase-space considerations are also taken into account and displayed in Fig. 8. Each phase-space for the different configurations is calculated generating a set of events with a random distribution, between the reaction products, of the energy and momentum available. The experimental detection limits, such as geometry and efficiency, are applied to the output events. Finally, the resulting distributions are normalized to the experimental yield for a direct comparison. Panel (a) in Fig. 8 shows that six-body $^{13}\mathrm{N} + {}^{3}\mathrm{H} + 4n$ phase-space of the ^{7}H channel starts to be appreciable around 10 MeV above the $^{3}\mathrm{H} + 4n$ threshold. The same panel also displays, for reference, a extreme case of three body phase-space involving a bound tetraneutron, $^{13}\mathrm{N} + {}^{3}\mathrm{H} + {}^{4}n$. The low lying character of the resonance ^{7}H allows to detect some events very close to the $^{3}\mathrm{H} + 4n$ decay threshold, which then may appear at negative energies due to the uncertainty in the excitation energy reconstruction. In the case of ^{6}H the six-body phase-space coming from ^{7}H begins to contribute around 10 MeV above the $^{3}\mathrm{H} + 3n$ threshold, while the five-body $^{14}\mathrm{N} + {}^{3}\mathrm{H} + 3n$ phase-space appears at 15 MeV, as well as the four-body $^{15}\mathrm{N} + {}^{3}\mathrm{H} + 2n$ phase-space coming from ^{5}H. This results in an estimated contamination below one count in the region corresponding to the ^{6}H peak.

Under these considerations those events located in the marked regions of panels (b) and (c) of Fig. 7 are identified as ^{6}H and ^{7}H production reactions, resulting in three and seven events among the total data.

B. Extraction of ^{6}H and ^{7}H resonance parameters

The production cross sections of ^{6}H and ^{7}H were determined as the number of detected events normalized to the number of incident projectiles and target nuclei. This calculation is corrected by the efficiency of the detection system and the efficiency in the event reconstruction procedure. The tracking process is strongly dependent on the ranges and angles of the trajectories to be reconstructed, producing different values of its associated efficiency depending on the kinematics of the detected reactions. Both contributions, from detection and event reconstruction, were explored for different

channels of reaction. The final efficiency results in 28% for reactions involving a ^{3}H detected in the CsI wall. The major contributions to this number arise from a strong cut in the reaction plane angle, with $|\phi| < 60^\circ$, and from the tracking process, which successfully reconstructs ∼40%; of the events corresponding to the channels of interest. Finally, a mean differential cross section of $\mathrm{d}\sigma/\mathrm{d}\Omega = 18.7^{+62.1}_{-13.3}$ μb/sr for ^{6}H and $\mathrm{d}\sigma/\mathrm{d}\Omega = 40.1^{+58.0}_{-30.6}$ μb/sr for ^{7}H, was obtained within the detection limits of MAYA, which explores different angular coverages in the center of mass system depending on the reaction. In the cases of ^{6}H and ^{7}H the angular coverages correspond to 8.7–46.2° and 9.7–48.2°, respectively.

The peak in excitation energy corresponding to the production of ^{7}H and ^{6}H resonances is described in this work with a modified Breit-Wigner distribution [29]:

$$\sigma_{\mathrm{BW}} = \sigma_0 \frac{\Gamma\sqrt{\frac{E^{\mathrm{exc}}}{E_R}}}{(E^{\mathrm{exc}} - E_R)^2 - \frac{\Gamma^2}{4}\frac{E^{\mathrm{exc}}}{E_R}}, \tag{5}$$

where the production cross section, σ_{BW}, depends on the excitation energy, E^{exc}, through the resonance energy, E_R, and width, Γ. The term $\sqrt{\frac{E^{\mathrm{exc}}}{E_R}}$ takes into account the energy dependence of the system barrier. The factor σ_0 is determined with the normalization to the total cross section.

The Breit-Wigner function is fitted to the experimental values of the excitation energy using a multiparametric maximum likelihood procedure, which is especially suited to low statistics samples. This procedure searches for the set of E_R and Γ parameters associated to the fitted function that better reproduces all the detected events. Each event probability contributes to the total likelihood as a Gaussian function, $\mathscr{G}_i$, centered in the measured excitation energy and with a variance equal to its calculated uncertainty, convoluted and normalized with the Breit-Wigner distribution:

$$P_i = \frac{\int \sigma_{\mathrm{BW}}(E_R, \Gamma) \otimes \mathscr{G}_i \, \mathrm{d}E^{\mathrm{exc}}}{\int \sigma_{\mathrm{BW}}(E_R, \Gamma) \, \mathrm{d}E^{\mathrm{exc}}}. \tag{6}$$

The total likelihood, $\mathscr{L}$, is calculated in an event-by-event basis, multiplying the individual probabilities, P_i. The optimal set of E_R and Γ is that one which maximizes the total likelihood:

$$\max[\mathscr{L}(E_R, \Gamma)] = \max\left[\prod_i P_i\right]. \tag{7}$$

The uncertainty associated to each event is mainly dominated by the tracking reconstruction process, varying from more than 6 to less than 1 MeV, with an average value of 2.5 MeV. The contribution of the estimated uncertainty is reflected in the final errors associated to the resonance width calculated by the likelihood procedure. The energy and width of the resonance are scanned until the maximum likelihood is found. Figure 9 shows the multiparameter surfaces corresponding to the search of the maximum likelihood for ^{6}H and ^{7}H. Once the maximum is located for each resonance, the uncertainty associated with the corresponding set of parameters is calculated as the variance of the distribution projected on each parameter. The sample stability is tested

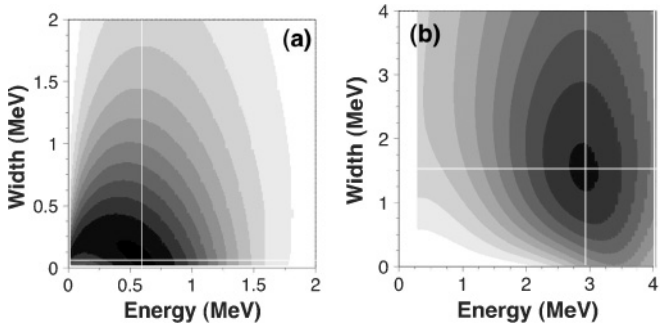

FIG. 9. Determination of maximum likelihood. The likelihood as a function of the energy and width of the resonance is plotted for (a) ^{7}H and (b) ^{6}H. The white lines correspond to the energy and width at the maximum likelihood in both cases.

in two different ways: In the first one, the fitting process is repeated with the different $N-1$ subsets of the total N events. The fitted parameters for each subset are within the uncertainty of the original parameters fitted from the total data set, assuring the stability of the fitting process respect to the number of detected events. In the second test, the sample stability is also investigated with respect to changes in the uncertainties of the calculated points. For this, the fit is performed applying different scaling factors to the original uncertainties, producing small variations around the original parameters, always within the uncertainty limits.

The fitted parameters result in a width of $\Gamma = 1.52^{+1.77}_{-0.35}$ MeV, and a resonance energy of $E_R = 2.91^{+0.85}_{-0.95}$ MeV above the threshold of the $^3\mathrm{H} + 3n$ subsystem for the ^{6}H resonance. The ^{7}H is found with a width of $\Gamma = 0.09^{+0.94}_{-0.06}$ MeV, and a resonance energy of $E_R = 0.57^{+0.42}_{-0.21}$ MeV above the threshold of the $^3\mathrm{H} + 4n$ subsystem. In Fig. 10 the fitted Breit-Wigner distributions of ^{6}H and ^{7}H are displayed with the experimental excitation energy distribution of detected events.

IV. DISCUSSION OF RESULTS

The extracted values for the energy and width of the ^{6}H resonance are in good agreement with those reported via ^{7}Li(^{7}Li, ^{8}Be)^{6}H at 82 MeV in [14], and ^{9}Be(^{11}B, ^{14}O)^{6}H

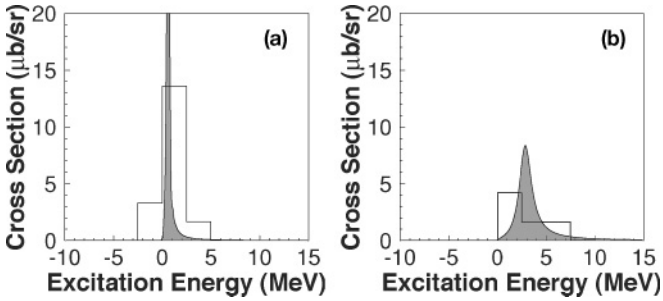

FIG. 10. Excitation energy distribution for the identified (a) ^{7}H and (b) ^{6}H events. The solid function is the Breit-Wigner distribution resulting from the fit to the experimental events. The data is represented with the empty histograms, merely as a guide to the eye, with a 2.5 MeV binning corresponding to the average estimated uncertainty.

in [10], with $E_R = 2.7 \pm 0.4$ MeV and $\Gamma = 1.8 \pm 0.5$ MeV in the first case, and $E_R = 2.6 \pm 0.5$ MeV and $\Gamma = 1.3 \pm 0.5$ MeV in the second reference. The difference in cross section, tenths of nb/sr compared with μb/sr found in this work, is likely to be due to the different transfer channels used to populate the ^{6}H resonance. However, there exist clear discrepancies with experiments involving pions: In [15] the resonance was not observed, while in [16] several states were found but no one comparable to those in transfer reactions. A difference of more than 4 MeV can be found between the ~2.7 ground state of [14] and [10] and the lower state, close to 7 MeV, of [16]. The authors in [16] are aware of some effects of final-state interaction that can be important in the stopped pion absorption and affect the detection near kinematical thresholds. These effects can be responsible for the loss of other low-lying states candidates to ground state.

The discrepancies between the experimental results, including the present one, may be resolved considering them as complementary data sets, where the ground state is likely to be around 2.7 MeV with a width of 1.5 MeV and a collection of excited states as observed in [16]. From the theoretical point of view, there is no satisfactory description of the properties of ^{6}H yet, being the closest theoretical predictions using an extended antisymmetrized molecular dynamics (AMD) approach [1]. There, the associated binding energy is calculated in -1.8 MeV, corresponding to 6.6 MeV above the $^3\mathrm{H} + 3n$ mass, which is almost 4 MeV over the present results. A clear overestimation is also found in their predicted binding energies of the rest of the hydrogen chain. This fact is pointed out by the authors as a systematic behavior that may be fixed adding other configurations of the nuclei structure in the calculation process.

Concerning the ^{7}H, a first discussion of the results can be found in [20]. In summary, the reported characterization of the resonance is in qualitative agreement with the previous experimental hint from [19]. The discussion can be extended with a recent work [16] where, as in the case of ^{6}H, a collection of excited states associated with the ^{7}H system in the $^9\mathrm{Be}(\pi^-, pp)^7\mathrm{H}$ reaction, and a broad structure close to the $^3\mathrm{H} + 4n$ mass in the missing mass spectrum of $^{11}\mathrm{B}(\pi^-, p^3\mathrm{He})^7\mathrm{H}$ are described. However, the same problems associated with final-state interactions prevent the authors from reporting the observation of the ground state for the system. Both sets of data can be again seen as complementary, with ground and excited states without experimental contradiction. The coexistence of these results may suggest a possible misinterpretation of the ^{6}H state reported in the present work from an excited state of ^{7}H. However, this scenario vanishes when any of the states found in [16], at 16 and 21 MeV, fits in the region where ^{6}H events lie on the ^{7}H excitation energy distribution (see Fig. 7). A theoretical description based on no-core approximation in the shell model predicts an excited level for the ^{7}H close to 6 MeV [17], in the region where ^{6}H is identified, but the same model fails in predicting the known levels of ^{5}H. Also, predictions for ^{6}H and ^{7}H ground states vary from bound systems with 4 and 6 MeV of binding energy to unbound resonances of -3 and -2 MeV, respectively, showing a reduced reliability of the model concerning hydrogen resonances properties. In addition, the extremely good agreement of the extracted values for the ground state of ^{6}H in this work with previous measurements remains as a strong argument against the possibility of being a ^{7}H excited state.

Regarding theoretical descriptions, AMD predicts a binding energy almost 7 MeV lower than the present results. Calculations based on a *hyperspherical functions method* applied on a shell model basis were reported as the closest to the present work, with resonance energies between 1 MeV [7] and 3 MeV [8]. This model reproduces in good approximation the isotopic chain of hydrogen with the exception of ^{6}H, to which the authors do not provide any result.

Being the resonance width related to the decay rate and mechanism, the relatively low value extracted in this work may be a hint of a fast and unique four-neutron decay [19,30]. Future studies of the ^{7}H nuclear state structure may bring more information about a possible four-neutron cluster, also interesting for the current discussion about the existence of tetra-neutron (^4n) state [31,32]. In addition, the low-lying character of ^{7}H, with a resonance energy close to the binding limit in less than 600 keV, and a relatively small width, opens an interesting question on the evolution of the properties in the next members of the hydrogen chain.

ACKNOWLEDGMENTS

This work was supported by grants from the Spanish Ministry of Education and Science, project FPA2005-00732, the CICYT-IN2P3 cooperation, and the Marie Curie Actions program support.

[1] S. Aoyama and N. Itagaki, Nucl. Phys. **A738**, 362 (2004).
[2] P. Navrátil, J. Vary, and B. R. Barrett, Phys. Rev. Lett. **84**, 5728 (2000).
[3] G. Blanchon, A. Bonaccorso, and N. Vinh Mau, Nucl. Phys. **A739**, 259 (2004).
[4] P. Descouvemont and A. Kharbach, Phys. Rev. C **63**, 027001 (2001).
[5] K. Arai, Phys. Rev. C **68**, 034303 (2003).
[6] A. Volya and V. Zelevinsky, Phys. Rev. Lett. **94**, 052501 (2005).
[7] N. K. Timofeyuk, Phys. Rev. C **65**, 064306 (2002).
[8] N. K. Timofeyuk, Phys. Rev. C **69**, 034336 (2004).
[9] E. Argan *et al.*, Phys. Rev. Lett. **9**, 405 (1962).
[10] A. V. Belozyorov *et al.*, Nucl. Phys. **A460**, 352 (1986).
[11] S. I. Sidorchuk *et al.*, Phys. Lett. **B594**, 54 (2004).
[12] M. Meister *et al.*, Phys. Rev. Lett. **91**, 162504 (2003).
[13] A. A. Korsheninnikov, M. S. Golovkov, I. Tanihata, A. M. Rodin, A. S. Fomichev, S. I. Sidorchuk, S. V. Stepantsov, M. L. Chelnokov, V. A. Gorshkov, D. D. Bogdanov, R. Wolski, G. M. Ter-Akopian, Y. T. Oganessian, W. Mittig, P. Roussel-Chomaz, H. Savajols, E. A. Kuzmin, E. Y. Nikolskii, and A. A. Ogloblin, Phys. Rev. Lett. **87**, 092501 (2001).
[14] D. Aleksandrov *et al.*, Sov. J. Nucl. Phys. **39**, 323 (1984).
[15] B. Parker *et al.*, Phys. Lett. **B251**, 483 (1990).
[16] Y. B. Gurov, Eur. Phys. J. A **32**, 261 (2007).

[17] N. A. F. M. Poppelier, L. D. Wood, and P. W. M. Glaudemans, Phys. Lett. **B157**, 120 (1985).
[18] A. M. Gorbatov *et al*., Sov. J. Nucl. Phys. **50**, 962 (1989).
[19] A. A. Korsheninnikov *et al*., Phys. Rev. Lett. **90**, 082501 (2003).
[20] M. Caamaño *et al*., Phys. Rev. Lett. **99**, 062502 (2007).
[21] A. C. C. Villari *et al*., Nucl. Phys. **A588**, 267c (1995).
[22] W. Mittig *et al*., Nucl. Phys. **A722**, 10c (2003).
[23] C. E. Demonchy *et al*., Nucl. Instrum. Methods A **573**, 145 (2007).
[24] C. E. Demonchy *et al*., Nucl. Instrum. Methods A **583**, 341 (2007).
[25] K. Lau and J. Pyrlik, Nucl. Instrum. Methods A **366**, 298 (1995).
[26] J. F. Ziegler, http://www.srim.org (2005).
[27] I. Endo *et al*., Nucl. Instrum. Methods **188**, 51 (1981).
[28] G. F. Knoll, *Radiation Detection and Measurement* (J. Wiley and Sons, Inc., New York, 1989).
[29] G. Breit and E. Wigner, Phys. Rev. **49**, 519 (1936).
[30] A. A. Korsheninnikov, Nucl. Phys. **A751**, 501c (2005).
[31] F. M. Marqués *et al*., Phys. Rev. C **65**, 044006 (2002).
[32] S. C. Pieper, Phys. Rev. Lett. **90**, 252501 (2003).